Journal of
MATERIALS RESEARCH

Welcome Comments Help

Nanostructured high-temperature superconductors: Creation of strong-pinning columnar defects in nanorod/superconductor composites

Peidong Yang and Charles M. Lieber
Division of Engineering and Applied Sciences, and Department of Chemistry, Harvard University, Cambridge, Massachusetts 02138

(Received 14 April 1997; accepted 10 June 1997)

A chemical approach to the formation of columnar defects involving the growth and incorporation of MgO nanorods into high temperature superconductors (HTS's) has been developed. MgO nanorods were incorporated into $Bi_2Sr_2CaCu_2O_z$, $Bi_2Sr_2Ca_2Cu_3O_z$, and $Tl_2Ba_2Ca_2Cu_3O_z$ superconductors at areal densities up to $2 \times 10^{10}/cm^2$. Microstructural analyses of the composites demonstrate that the MgO nanorods create a columnar defect structure in the HTS matrices, form a compositionally sharp interface with the matrix, and self-organize into orientations perpendicular and parallel to the copper oxide planes. Measurements of the critical current density demonstrate significant enhancements in the MgO nanorod/HTS composites at elevated temperatures and magnetic fields compared with reference samples.

I. INTRODUCTION

Large critical current densities (J_c's) are essential to many proposed applications of HTS's, such as wires for power transmission cables and solenoids.[1,2] Consequently, enhancing J_c in HTS materials has been and remains a topic of great scientific and technological interest. In general, J_c is limited by both intrinsic and extrinsic factors.[1,3,4] For example, J_c is limited by thermally activated flux flow (TAFF); that is, J_c vanishes well below the upper critical field line $H_{c2}(T)$ as a result of the motion of magnetic flux lines. This limitation is intrinsic, and arises from the short coherence lengths and large anisotropies of the HTS materials that lead to weak pinning of flux lines.[3–6] In the polycrystalline materials used for large-scale applications, J_c is also limited by extrinsic factors such as the interfaces between superconducting grains and the development of microcracks during processing.[3,7] Poor alignment of crystalline grains and chemical heterogeneity at their boundaries, as well as microcracks, produce weak links with low values of J_c. Over the past several years, significant progress has been made in improving the alignment of grains and consequently improving J_c's in wires and tapes based on $Ag–Bi_2Sr_2Ca_{n-1}Cu_nO_{2n+4}$ ($n = 2$, BSCCO-2212; $n = 3$, BSCCO-2223), and $YBa_2Cu_3O_z$ (YBCO) by identifying how material processing conditions affect microstructure and transport currents.[3,8–10] Despite this progress in processing, which is now yielding BSCCO-based wires with J_c values sufficiently high for some commercial applications[10] and exciting performance in aligned YBCO tapes,[9] the intrinsic problem of TAFF remains a limitation to the performance of HTS materials at high temperatures and magnetic fields.[11–13]

The traditional method of flux line pinning to reduce TAFF in conventional type-II superconductors, which involves introducing point-like defects into the superconductor matrix, has been ineffective in the HTS's. Theoretical and experimental work has shown, however, that the problem of TAFF in HTS's can be reduced significantly by creating correlated defects, such as columnar defects, in the crystal lattice.[14–17] The interaction of flux lines with columnar defects results in a large pinning energy that effectively resists thermally activated motion, and thus increases J_c significantly at high temperatures and magnetic fields (Fig. 1).[14,18] Significantly, columnar defects improve J_c in both BSCCO and YBCO superconductors,[16,18] and thus have the potential to become a key technological tool in the fabrication of high J_c wires. These line-like defects are usually created by irradiating samples with heavy ions having energies on the order of a billion electron volts (GeV). This procedure yields amorphous damage tracks 10 to 20 nm in diameter and tens of micrometers in length.[19] The small defect diameter is essential to maximize the flux line core-pinning interaction without destroying an unnecessary volume fraction of the superconductor. Although the effectiveness of heavy-ion generated columnar defects in enhancing J_c has been clearly demonstrated,[16–18] the suitability of this technique for large-scale applications is limited by the short penetration depth of heavy ions and the low thermal stability of the defects.[20] These factors eliminate the possibility of producing columnar

 © 1997 Materials Research Society

CAMBRIDGE JOURNALS
http://journals.cambridge.org Downloaded: 30 Oct 2015 IP address: 128.103.96.231

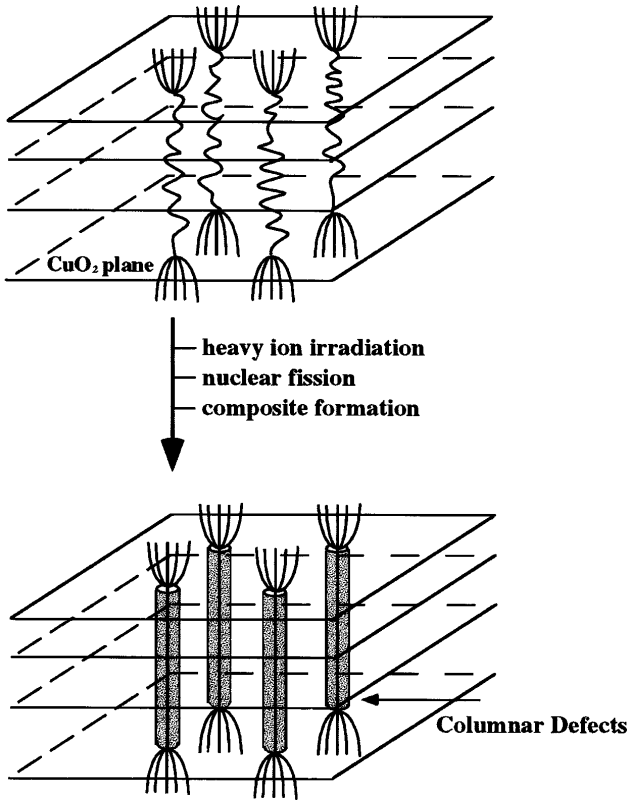

FIG. 1. Schematic diagram illustrating magnetic flux lines in a HTS before and after the creation of columnar defects. The linear defects, which can be made by heavy ion irradiation, nuclear fission, and nanorod composite formation, strongly pin the flux lines in the superconductor.

defects in processed wires or of forming wires from irradiated BSCCO powders, respectively. However, GeV protons can be used to create isotropic columnar damage tracks in BSCCO materials through the fission of Bi nuclei.[21,22] The advantage of this approach is the large, 0.5 m penetration depth of the energetic protons that makes possible the production of columnar defects in completed wire cables. The fission process does, however, produce an isotropic distribution of defects that reduces the pinning efficiency of the columnar defects,[15] and produces radioactive daughter nuclei that may make this approach unattractive to the public at large. Furthermore, it is unclear whether high-energy, ion-irradiation techniques are economically viable for large-scale commercial applications.

The large enhancement of J_c produced by columnar defect structures argues that other strategies should be considered for their creation in HTS materials.[23] For example, the incorporation of rod-like nanostructures into a HTS matrix should yield the same beneficial effect as ion-generated columnar defects. There are, however, several critical constraints to achieving a useful columnar defect structure in a composite. First, the rod-like structures must have diameters comparable to ion damage tracks or the coherence length of the HTS's (i.e., nanorods) so that they effectively pin the flux lines while at the same time minimizing the nonsuperconducting phase in the HTS matrix. Second, the nanorods should be chemically inert in the aggressive metal oxide environment used to prepare HTS's; otherwise, the nanorods will not create columnar defects and may have adverse effects on the superconducting properties due to the incorporation of impurity ions in HTS lattice. Third, the nanorods should be oriented within the superconducting matrix to maximize the pinning efficiency. From the perspective of size, carbon nanotubes and carbide nanorods are materials that could be considered for creating columnar defects.[24,25] Carbon nanotubes are, however, oxidized to carbon dioxide gas in the oxygen-metal oxide environment used to prepare high-quality samples, and thus are not useful for introducing a high density of well-defined columnar defects. Likewise, carbide nanorods[25] also react with the HTS matrix and severely degrade the superconducting properties.

This key issue of chemical reactivity has led us to focus on the growth of nanorods of simple inert oxide materials such as MgO, and their subsequent incorporation into HTS's.[26] MgO has been found to be chemically compatible with most HTS's and is widely used as a substrate for HTS thin films and as a crucible material for the growth of HTS single crystals. Previous studies of micrometer-diameter MgO whiskers have shown that this material can be incorporated into BSCCO superconductors with little chemical reaction.[27,28] The principal effect of these micron size whiskers is an improvement in mechanical properties; J_c does not appear to be enhanced and in some cases is lowered by their addition.[28] Presumably the reduction of J_c is due to a decrease in the cross-sectional superconducting area in the composite, the inhibition of grain growth of the BSCCO phase, and the interference of grain alignment in the presence of the large whiskers. In contrast, we have recently found that large enhancements in J_c can be achieved by using nanometer size MgO single crystal whiskers termed nanorods.[26,29,30] Herein we describe in detail the growth and structural properties of MgO nanorods and nanorod composites formed with thick film and bulk BSCCO-2212, BSCCO-2223, and $Tl_2Ba_2Ca_2Cu_3O_z$ (TBCCO-2223) HTS materials. Magnetization measurements made on these samples demonstrate that the nanorod/HTS composites exhibit enhancements in J_c similar to those produced previously by high-energy ion irradiation. Our approach to overcoming the intrinsic limitation of thermally activated flux flow can be implemented in processes currently used to produce large-scale HTS samples and thus might be useful in applications such as power transmission cables.

CAMBRIDGE JOURNALS
http://journals.cambridge.org Downloaded: 30 Oct 2015 IP address: 128.103.96.231

II. EXPERIMENTAL SECTION

A. Growth of MgO nanorods

The MgO nanorods were prepared using a modified vapor-solid crystal growth process. Briefly, a mixture of MgO powder (200 mesh, Alfa AESAR) and carbon powder (300 mesh, Johnson Matthey) in a 1 : 3 weight ratio was placed at the center of a tube furnace within a graphite boat. The mixture was heated to approximately 1200 °C under a flow of high purity argon to generate magnesium vapor which is then transported to nucleation sites located downstream from the MgO/carbon mixture. The nanorod growth time was typically between 5 and 30 min. Two types of nucleation sites have been used to produce nanorods: (1) nanoscale etch pits/hillocks and (2) MgO nanocrystallites. The nanoscale pits/hillocks were created by etching MgO (001) substrates in 0.5 M $NiCl_2$ solutions for 1 to 30 min. Alternatively, MgO nanocrystallites were prepared using a previously reported method[31] or deposited *in situ*. Additional details about the growth and structure of the MgO nanorods are described in Sec. III. A.

B. Preparation of nanorod/HTS composites

To prepare textured thick film BSCCO-2212 composites, pulsed laser deposition (PLD) was first used to deposit 1–5 μm BSCCO films onto substrates on which oriented MgO nanorods had been previously grown (Fig. 2). The BSCCO-2212 PLD targets were made by grinding a stoichiometric ratio of Bi_2O_3, $SrCO_3$, $CaCO_3$, and CuO, compacting this mixture into a pellet and then sintering to form a dense target. A Nd:YAG laser (532 nm) was used to ablate this target using a fluence of approximately 1 J/cm^2.[32] The BSCCO films were deposited in 50–200 mTorr of oxygen with substrate temperatures of 25 and 650 °C. Next, the thick films produced in this way were partially melted in a tube furnace at 880 °C for 15 min, and then slowly cooled to form textured superconducting thick films.[33] Films prepared by deposition at both temperatures exhibited similar texture, although microcracks were reduced in samples deposited at 650 °C.[34] Nanorod/BSCCO-2223 composite films were prepared by laser deposition of $Bi_{1.8}Pb_{0.3}Sr_2Ca_2Cu_3O_z$ targets at 680 °C followed by annealing at 800–810 °C in air.[35] The as-prepared BSCCO-2212 and 2223 samples were then post-annealed in flowing Ar at 350 °C for 3 h to optimize the superconducting transition temperature, T_c. Reference samples without nanorods were prepared using similar procedures for the purpose of comparison.

Textured Tl-2223 film composites were prepared by a two-stage process that involves (1) PLD of 1–2 μm thick amorphous $Ba_2Ca_2Cu_3O_z$ thick films at 200 °C followed by (2) *ex situ* thallination.[36] During the thallination process, the amorphous films were encapsulated

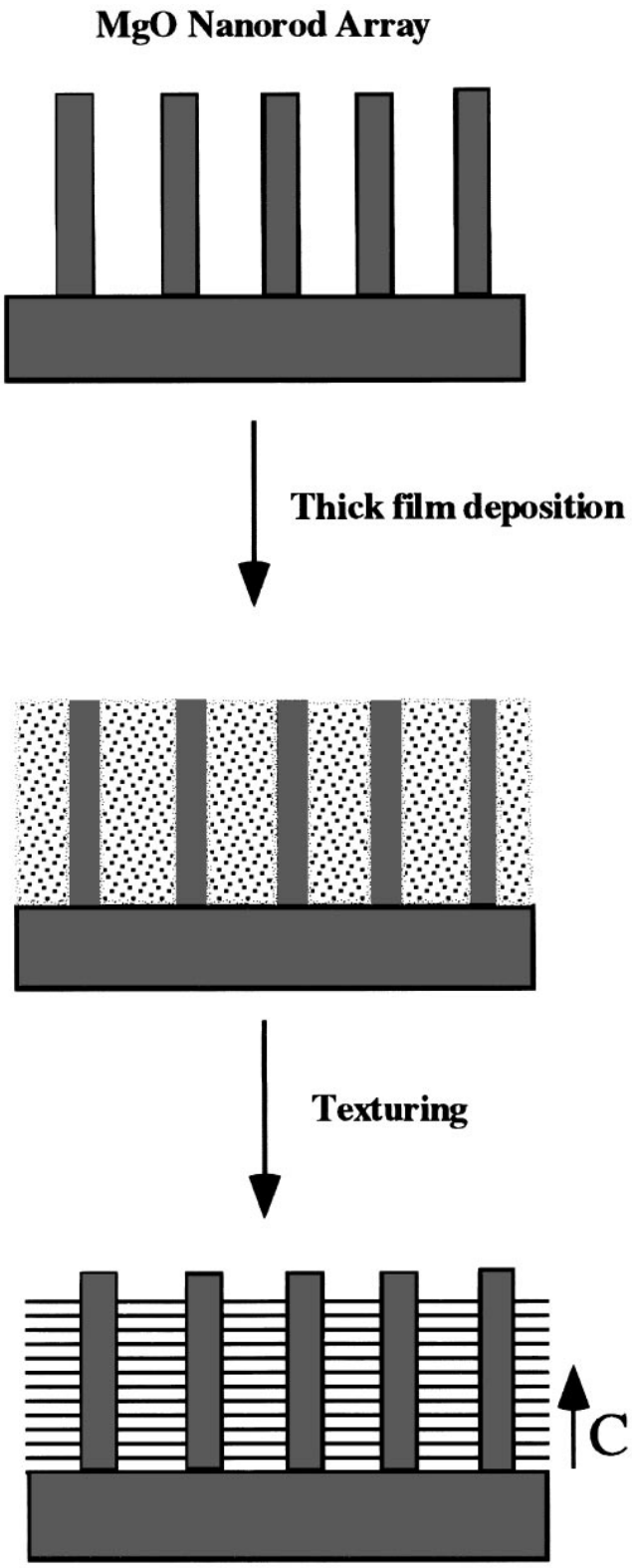

FIG. 2. Schematic diagram illustrating the preparation of a nanorod/HTS composite starting from a nanorod forest oriented on a substrate surface.

CAMBRIDGE JOURNALS
http://journals.cambridge.org Downloaded: 30 Oct 2015 IP address: 128.103.96.231

with TBCCO-2223 powder in Ag foils and placed in half-sealed alumina tubes with Tl_2O_3. The Tl source temperature was kept at 890 °C, while the film temperature was maintained at 790 °C. Reference samples without nanorods were also prepared using similar procedures.

In addition, bulk BSCCO-2212 composites have been prepared using a two-step process. First, 5–15% by weight bulk MgO nanorods were mixed homogeneously with prereacted BSCCO-2212 powder. Second, the nanorod/BSCCO-2212 mixture was partially melted on silver foil at 880 °C, and then slowly cooled to form a textured superconducting tape. Reference samples without nanorods were prepared using similar procedures.

C. Characterization of the nanorods and composites

The MgO nanorods and nanorod/HTS composites were analyzed using a variety of techniques to characterize their microstructure and J_c's. Scanning electron microscopy (JEOL, JSM 6400) was used to study the oriented growth of MgO nanorods on MgO single crystal substrates and the microstructure of as-deposited films, textured films, and bulk samples. Backscattered electron images were also obtained to map qualitatively elemental distributions on the surfaces of the composites. Transmission electron microscopy (Philips, EM420T) was used to study the growth behavior and size of the MgO nanorods and the local structure, orientation, and interfaces of the nanorod/HTS composites. In addition, spatially resolved energy dispersive x-ray spectroscopy (EDAX) was used to determine the local composition across the nanorod/HTS interface. The overall texture and crystallinity of the films were characterized using x-ray (Rigaku, D/Max) θ-2θ scans and rocking curve measurements.

Magnetization measurements were made using a superconducting quantum interference device (SQUID, Quantum Design MPMS1) to determine T_c and J_c. The Bean model, which relates a measured hysteresis in magnetization, $\Delta M(H, T)$, to the supercurrents flowing within the sample, was used to determine $J_c : J_c = 15\Delta M/R$, where R is the radius of the sample.[37] Although this approach could underemphasize the limitation of grain boundaries on J_c, it is appropriate for probing the intrinsic effects of defect pinning that are the focus of our studies.[11,21]

III. RESULTS AND DISCUSSION

A. Structure of MgO nanorods

Figure 3 shows cross-sectional SEM micrographs of MgO nanorods grown on etched MgO (100) substrates. Most of the rods are observed to grow normal to the substrate, and thus form what we have termed a nanorod forest.[26] High densities of nanorods can be grown on the substrates by this approach. For example, the nanorod density in Fig. 3(a) is $3 \times 10^9/\text{cm}^2$ and that in Fig. 3(b) is nearly a factor of ten larger, $2 \times 10^{10}/\text{cm}^2$. These densities correspond to effective matching fields of 600 and 4000 G, respectively. The true density of pinning sites is, however, likely to be much larger, as discussed previously.[26] Analyses of TEM micrographs recorded on nanorods cleaved from substrate surfaces and dispersed onto holely carbon grids (e.g., Fig. 4) show that the diameters of these rods range from 7 to 40 nm with an average of 15 nm. The lengths of the rods range from 1 to 3 μm. The rods thus have quite high aspect ratios. The nanorods also appear to have smooth surfaces and may be gently curved.

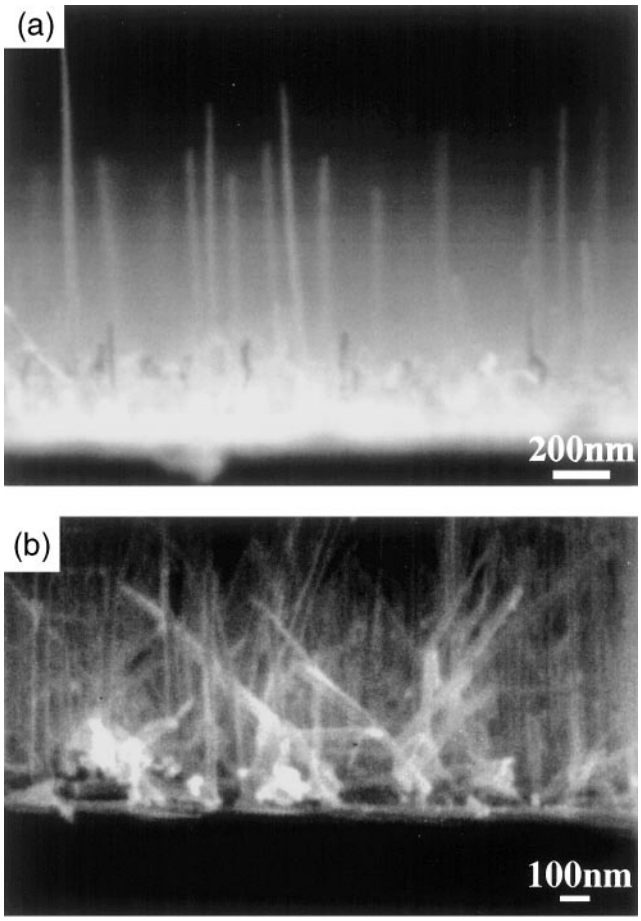

FIG. 3. Cross-sectional SEM images of MgO nanorod forests with areal densities of (a) $3 \times 10^9/\text{cm}^2$ and (b) $2 \times 10^{10}/\text{cm}^2$. The nanorods were grown on etched MgO (100) substrates at 1150 °C for 10 min.

The composition and structure of the nanorods was confirmed by EDAX and diffraction studies. EDAX data recorded on nanorods show no evidence for heavy elements other than Mg. In addition, convergent beam electron diffraction on isolated nanorods [Fig. 4(b)] and x-ray diffraction measurements on bulk samples (Fig. 5)

CAMBRIDGE JOURNALS
http://journals.cambridge.org Downloaded: 30 Oct 2015 IP address: 128.103.96.231

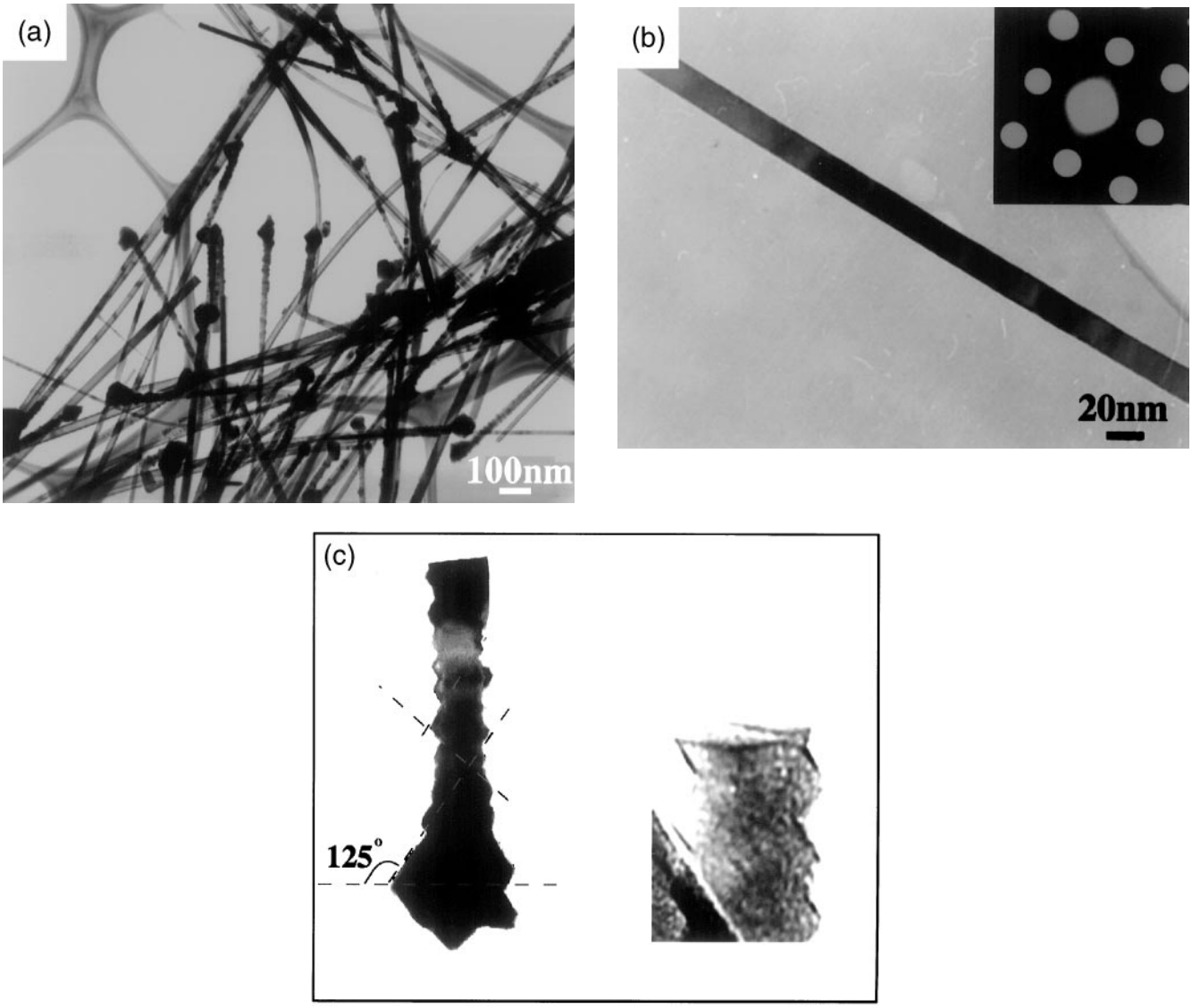

FIG. 4. (a) TEM micrograph of MgO nanorods cleaved from a MgO substrate. (b) TEM image of a single MgO nanorod. The ⟨100⟩ growth direction was determined from convergent beam electron diffraction (inset) recorded with the electron beam perpendicular to the nanorod axis. (c) Growth habits of the MgO nanorods. The initial nucleation site is shown on the left and a view of the square cross section of a fractured rod is shown on the right.

can be indexed to the cubic MgO lattice, and show no evidence for secondary phases.

Since MgO has an isotropic, cubic structure, it is somewhat surprising to observe the growth of highly anisotropic MgO nanorods. Detailed TEM experiments were carried out on the nanorods to elucidate possible growth mechanisms leading to these highly anisotropic structures. The growth axis of the MgO nanorods, which was determined using convergent beam electron diffraction [Fig. 4(b), inset], was found to be along the ⟨001⟩ direction in all samples studied. In addition, we found that one end of the nanorods typically terminated in an octahedrally shaped cluster and that the nanorods exhibited a zigzag morphology for several hundred nanometers past these sites before changing to the smooth morphology seen over the major portion of their lengths [Fig. 4(c)]. Furthermore, tilting experiments showed that the other ends of the nanorods are square [Fig. 4(c), inset]. Because the nanorod axis corresponds to the ⟨001⟩ direction, these square ends can be assigned to (100) surfaces. We believe that the octahedrally shaped clusters and zigzag morphology correspond to the nucleation sites and initial growth stage, respectively.

The above results suggest that nanorod growth proceeds through a vapor-solid mechanism analogous to that described previously for micron diameter whiskers.[38] In this mechanism, the nucleation site size is critical for defining the rod diameter when the vapor supersaturation

CAMBRIDGE JOURNALS
http://journals.cambridge.org Downloaded: 30 Oct 2015 IP address: 128.103.96.231

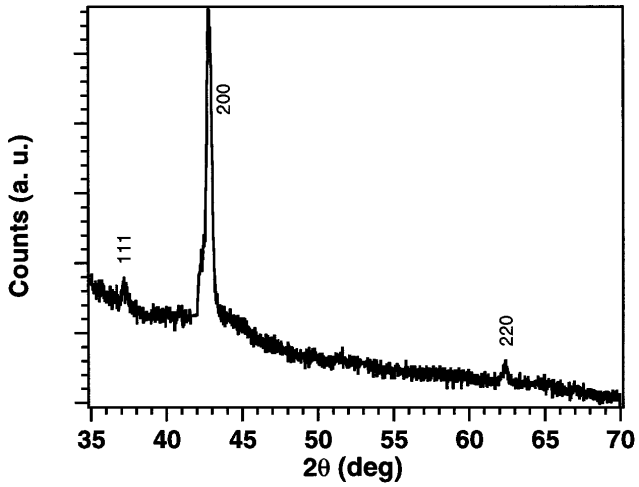

FIG. 5. X-ray diffraction pattern recorded on free-standing MgO nanorods cleaved from a substrate surface.

is appropriately controlled. The pits and hillocks created on MgO (100) substrates by etching thus appear to define the critical nanoscale nucleation sites. The observation of rod-like structures with cubic MgO also requires that the axial growth rate be greater than the overgrowth rate. In MgO, previous studies found that the growth rates increased from ⟨111⟩ to ⟨110⟩ to ⟨001⟩; these rate differences were suggested to reflect the decreasing solid-vapor interfacial free energy of the corresponding surfaces.[39] A model that explains qualitatively nanorod growth in light of these observations is proposed in Fig. 6. The nanorod growth can be divided into two stages after the initial nucleation. In the first stage beyond nucleation, growth along the ⟨001⟩ direction occurs with (111) side planes. In the second stage, the side planes smooth into (110) or (001) planes due to the smaller free energy associated with the lower index faces. These growth habits are also observed experimentally, as shown in Fig. 4(c). The ~55° angle measured between facets for this nanorod, which was imaged along the [110] zone axis, clearly indicates that the corrugation corresponds to (111) planes at the initial stage of growth. Figure 4(b) shows the second stage of the crystal growth in which faces are smooth and parallel to the growth direction. As discussed below, the growth habits of the MgO nanorods also serve an important function in the development of the local microstructure in the nanorod/superconductor composites.

The growth of unsupported MgO nanorods appears to proceed in a similar way with MgO nanocrystallites serving as the nucleation sites. These nanocrystallites are aggregates of polyhedral particles with kinks, steps, and truncated corners that expose high index crystal planes such as (111).[40] The nanocrystallites thus exhibit features similar to the pits and hillocks created on the MgO substrates by etching. Figure 7(a) shows a TEM image of nanorods nucleated and grown on 5–8 nm diameter

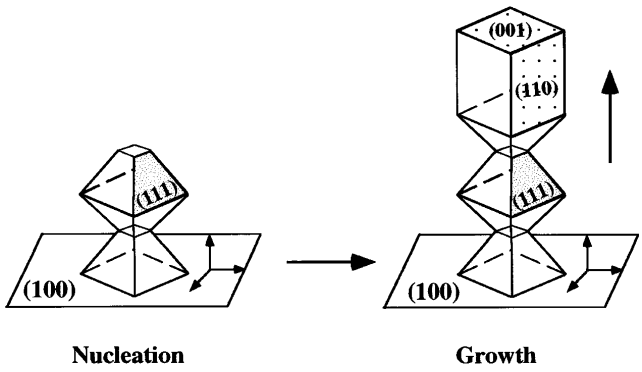

FIG. 6. Schematic diagram illustrating nucleation and growth of the MgO nanorods. The relevant crystallographic planes are highlighted.

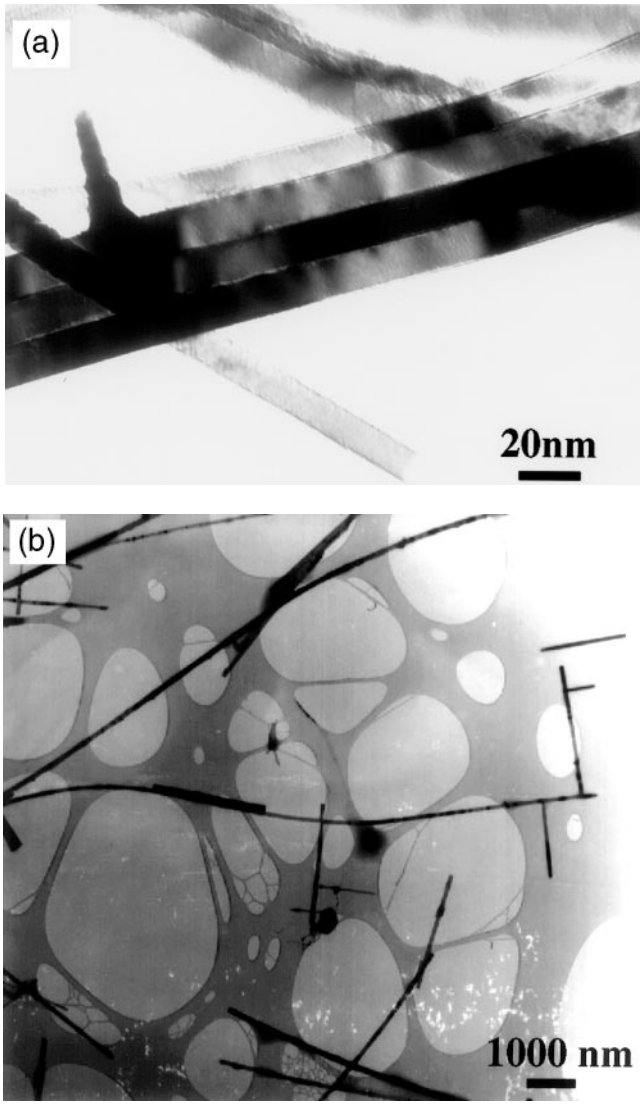

FIG. 7. TEM micrographs of unsupported MgO nanorods grown using (a) 5–8 nm and (b) 100 nm diameter nucleation sites.

CAMBRIDGE JOURNALS
http://journals.cambridge.org Downloaded: 30 Oct 2015 IP address: 128.103.96.231

MgO nanocrystallites. The diameters of the corresponding nanorods range from 8 to 50 nm with an average of 25 nm. These samples also exhibit a similar growth behavior (i.e., growth direction and habits) as those grown on the etched MgO (100) substrates. We have also used the growth of unsupported MgO nanorods to test the importance of nucleation in determining nanorod diameter. Nanorod growth using larger ~ 100 nm MgO crystallites for nucleation but otherwise identical reaction conditions produced nanorods with an average diameter of 80 nm [Fig. 7(b)]. Hence, it is clear that nucleation represents a critical step in the growth of the MgO nanorods.

B. Microstructure of the nanorod/HTS composites

In order to elucidate the phase formation and chemistry of nanorod/HTS composites, we have investigated composites prepared using the oriented nanorod forests grown on MgO substrates and unsupported MgO nanorods. The nanorod forests provide a particularly well-controlled environment for studying HTS composite formation since the positions and orientations of the nanorods are fixed by the substrate.

In general, high-quality nanorod/BSCCO-2212 composites and reference BSCCO-2212 samples have been made through the use of standard melt-texturing procedures[20,33] that produce polycrystalline samples with well-oriented (textured) grains. X-ray diffraction studies of the composites show that the partial melting-cooling cycle leads to crystalline, textured BSCCO-2212 [Fig. 8(a)] in which the crystallographic *c*-axis is normal to the substrate surface. Rocking curve analysis [Fig. 8(b)] of the composite and reference samples further shows that the nanorods do not adversely affect the development of a well-textured (FWHM $< 1°$) polycrystalline product. The columnar defect structure in the nanorod/BSCCO-2212 composite prepared on a $3 \times 10^9/\text{cm}^2$ MgO nanorod forest is observed clearly in SEM images (Fig. 9). First, low-magnification side-view images of nanorod/BSCCO composites prepared by PLD at low temperature exhibit a columnar morphology that reflects deposition around the forest of nanorods [Fig. 9(a)]. In contrast, reference samples prepared in a similar manner do not exhibit a columnar morphology. Second, images of melt-textured samples show the characteristic plate-like morphology of BSCCO and exhibit a density of nanorods protruding from the BSCCO surface ($1 \times 10^9/\text{cm}^2$) that is similar to the one measured on the substrate before composite formation [Fig. 9(b)]. Similar results were also obtained for BSCCO-2212 composites formed using a much higher $2 \times 10^{10}/\text{cm}^2$ density nanorod forest, as shown in Fig. 10. These results show that dense columnar defect arrays needed for effectively pinning flux lines at high fields are accessible using our approach. In addition, extended annealing studies at temperatures between 800 and 850 °C suggest that the nanorods do not react significantly with the BSCCO matrix on a time scale of 3 days (below the liquidus point).

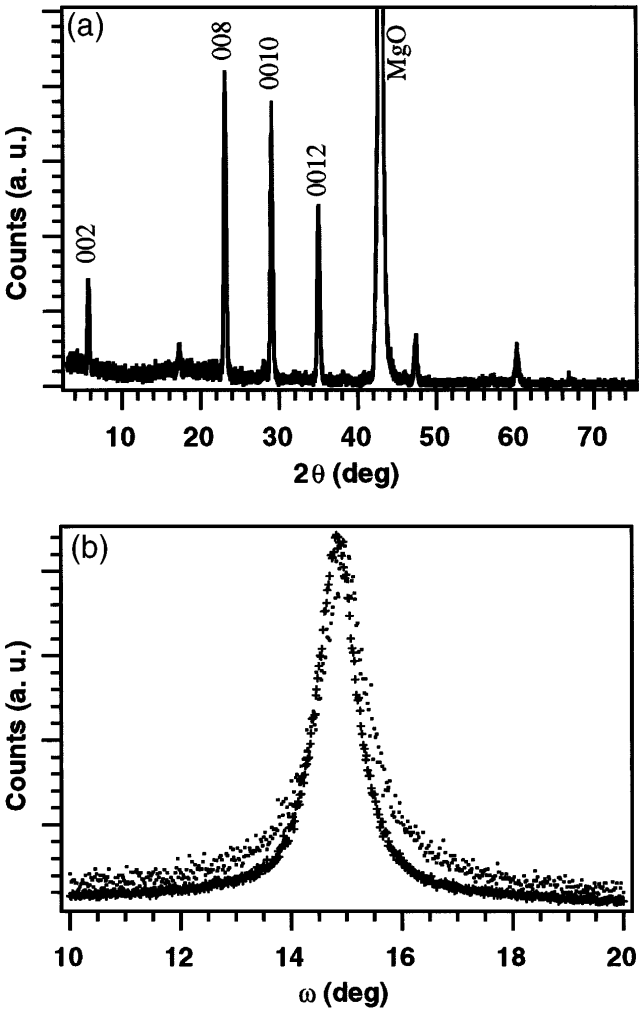

FIG. 8. (a) X-ray diffraction pattern recorded on a nanorod/BSCCO-2212 composite. Only the (001) BSCCO diffraction peaks are observed. (b) Rocking curves measured on the (0010) peak of composite (heavy crosses) and reference (lighter points) BSCCO-2212 samples.

We have also investigated the formation of nanorod/HTS composites using TBCCO-2223 and BSCCO-2223 materials. Structural studies of these composites show that in both systems the nanorods are incorporated into the superconductor crystal grains in a manner similar to the BSCCO-2212 system. For example, x-ray diffraction measurements made on a nanorod/TBCCO-2223 composite (Fig. 11) show that TBCCO is textured with the *c*-axis perpendicular to the substrate surface and that the sample is $>95\%$ phase pure. Similar diffraction patterns were recorded on composites formed using high-density nanorod forests as well. Cross-sectional SEM images of the

CAMBRIDGE JOURNALS
http://journals.cambridge.org Downloaded: 30 Oct 2015 IP address: 128.103.96.231

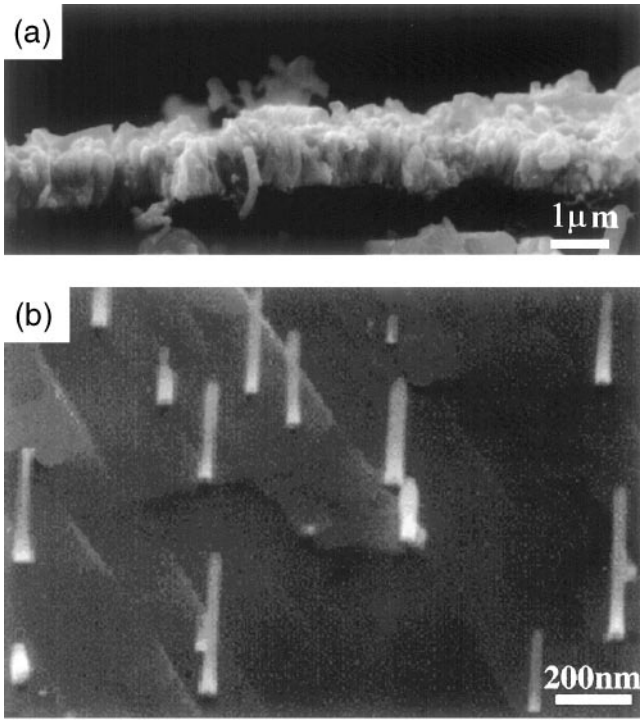

FIG. 9. (a) Cross-sectional SEM image of a nanorod/BSCCO-2212 composite before melt-texturing. (b) SEM image of the nanorod/BSCCO composite after texturing; the image was recorded at a 45° angle to the surface normal. The nanorods protruding from the BSCCO basal plane appear light gray.

$Ba_2Ca_2Cu_3O_z$ films show that the nanorod array is filled with amorphous $Ba_2Ca_2Cu_3O_z$, and that many nanorods are protruding from the free surface of the material [Fig. 12(a)]. After thallination and texturing, the superconducting composite films have a smooth plate-like morphology with a high density of nanorods protruding from the basal *a-b* plane of crystal grains [Fig. 12(b)]. The observed density of nanorods, $1 \times 10^9/\text{cm}^2$, corresponds well to the initial density of nanorods.

In addition, we have obtained similar results for nanorod/BSCCO-2223 composites. Figure 13 shows SEM images of reference and nanorod composite samples obtained after annealing BSCCO-2223 films at 815 °C for 48 h. These images exhibit similar BSCCO grain structure, and importantly, the presence of a high-density of nanorods protruding from individual grains in the composite. The 110 K T_c's determined for the reference and nanorod composite samples suggest strongly that BSCCO-2223 phase is formed; however, x-ray diffraction measurements do indicate the presence of a 5–10% impurity phase in the samples. We believe that these results are quite promising, although clearly additional work will be needed to optimize the microstructure in our nanorod/BSCCO-2223 composites.

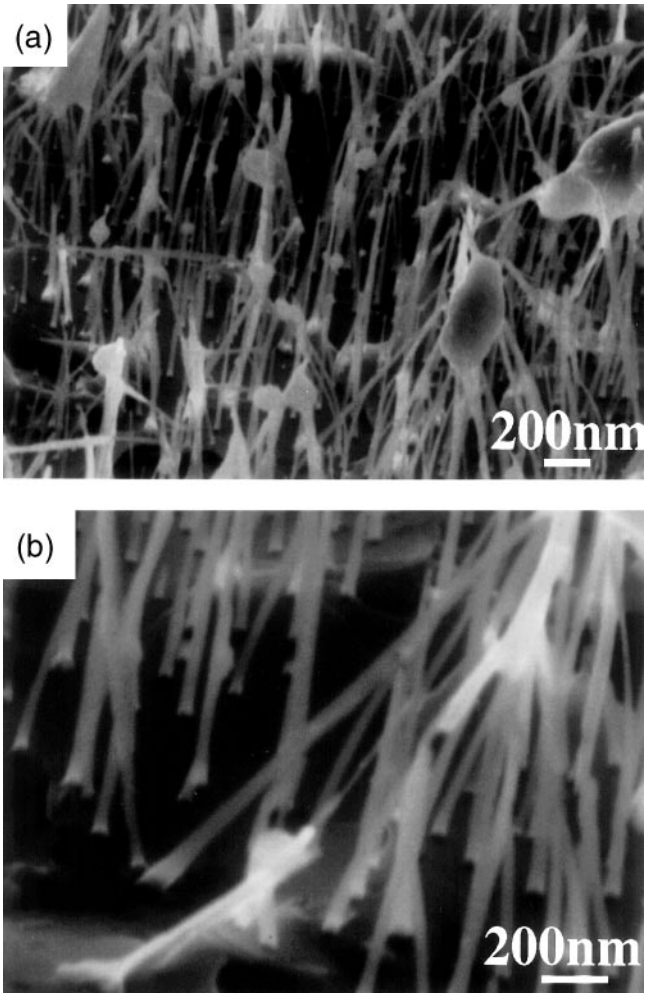

FIG. 10. SEM images recorded at (a) low- and high-magnification of a nanorod/BSCCO composite. The nanorods form a high density array in this composite.

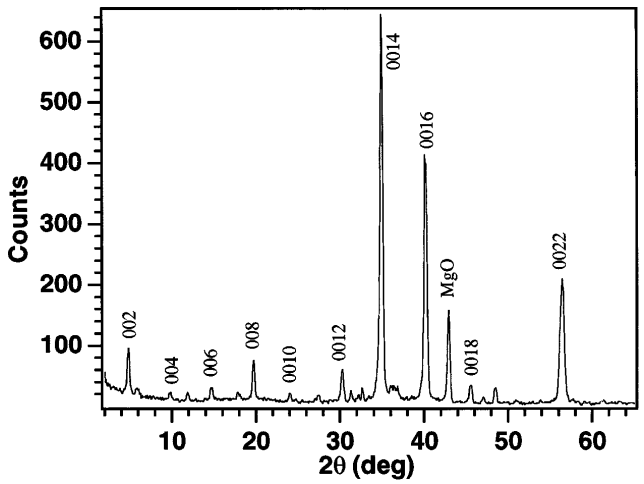

FIG. 11. X-ray diffraction pattern recorded on a textured nanorod/TBCCO-2223 composite.

CAMBRIDGE JOURNALS
http://journals.cambridge.org Downloaded: 30 Oct 2015 IP address: 128.103.96.231

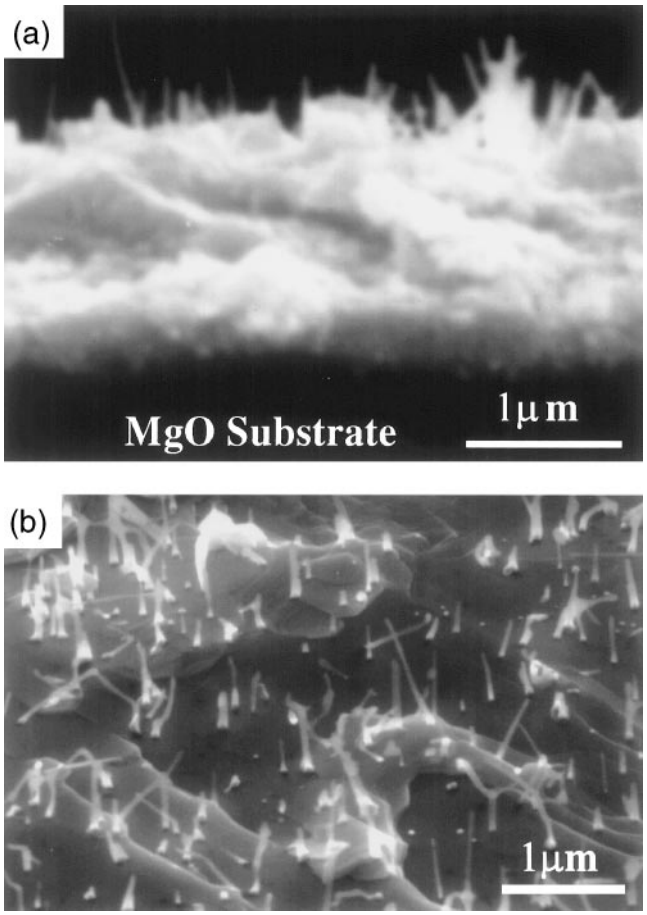

FIG. 12. (a) Cross-sectional SEM image of the first stage of composite formation after amorphous $Ba_2Ca_2Cu_3O_z$ was deposited onto a nanorod forest. (b) SEM image of a textured nanorod/TBCCO-2223 composite recorded at a 45° angle to the surface normal. MgO nanorods protruding from the surface appear light gray.

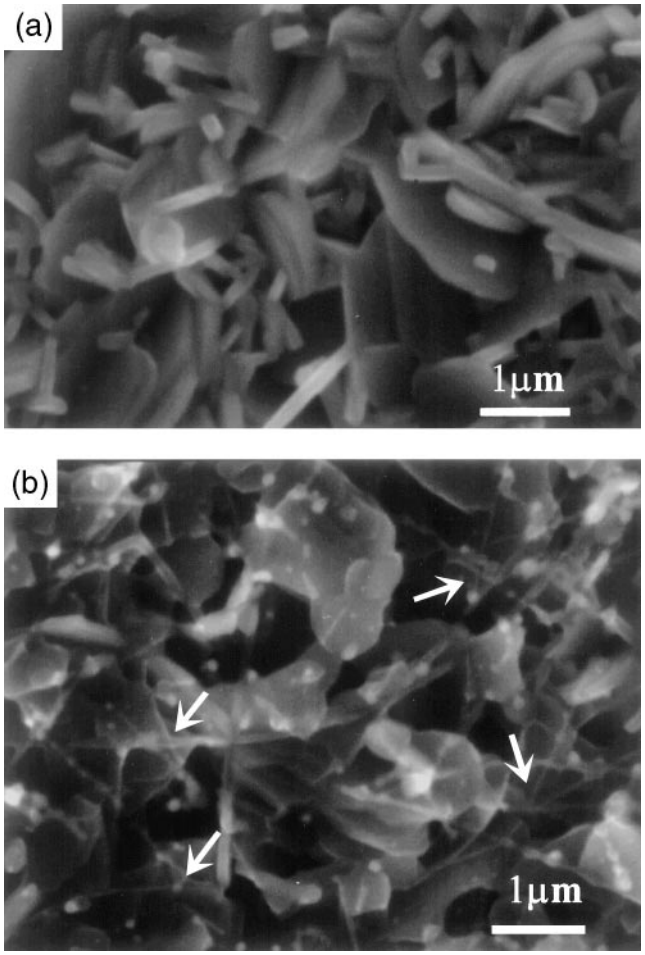

FIG. 13. (a) SEM micrograph of a reference BSCCO-2223 sample shows the small typical crystallites. (b) Typical SEM image of a nanorod/BSCCO-2223 composite shows that the MgO nanorods penetrate through the small crystallites; arrows highlight several clusters of penetrating nanorods.

Lastly, we have studied the formation of bulk nanorod/BSCCO-2212 composites. Composites prepared on silver tapes exhibited features similar to those described above for the film composites. X-ray diffraction measurements made on both composite and reference samples exhibited only the (001) reflections of BSCCO-2212, thus showing a good texture of the BSCCO grains within these samples. More importantly, TEM studies of these samples showed that a high density of MgO nanorods were incorporated into the crystalline grains (Fig. 14). Images recorded with the electron beam along the *c*-axis showed roughly circular, dark spots with diameters of 30 nm that contained primarily Mg. Selected area electron diffraction data recorded at the same time confirm the orientation of the observed MgO nanorods and BSCCO crystal grain [Fig. 14(b)]. These features are similar to those observed for the samples containing substrate-oriented nanorods, and thus suggest that many nanorods preferentially orient along the BSCCO-2212 *c*-axis in these silver tape samples. The columnar structure and near *c*-axis orientation of the nanorods were further confirmed by sample tilting experiments [Fig. 14(c)] and high-resolution cross-sectional images [Fig. 15(a)]. The high-resolution images show clearly the BSCCO layered structure (spacing $= c/2$) with the nanorod perpendicular to the layers. In addition, these TEM studies demonstrate that a large number of nanorods also orient preferentially in the BSCCO *a-b* plane [Fig. 14(d)]. The preferential orientation of nanorods is summarized in Fig. 16. Because oriented columnar defects are expected to produce improved values of J_c compared with an isotropic distribution,[15] we believe that the observed self-organization of MgO nanorods during composite processing is significant for applications. The origin of self-organization is discussed below.

CAMBRIDGE JOURNALS
http://journals.cambridge.org Downloaded: 30 Oct 2015 IP address: 128.103.96.231

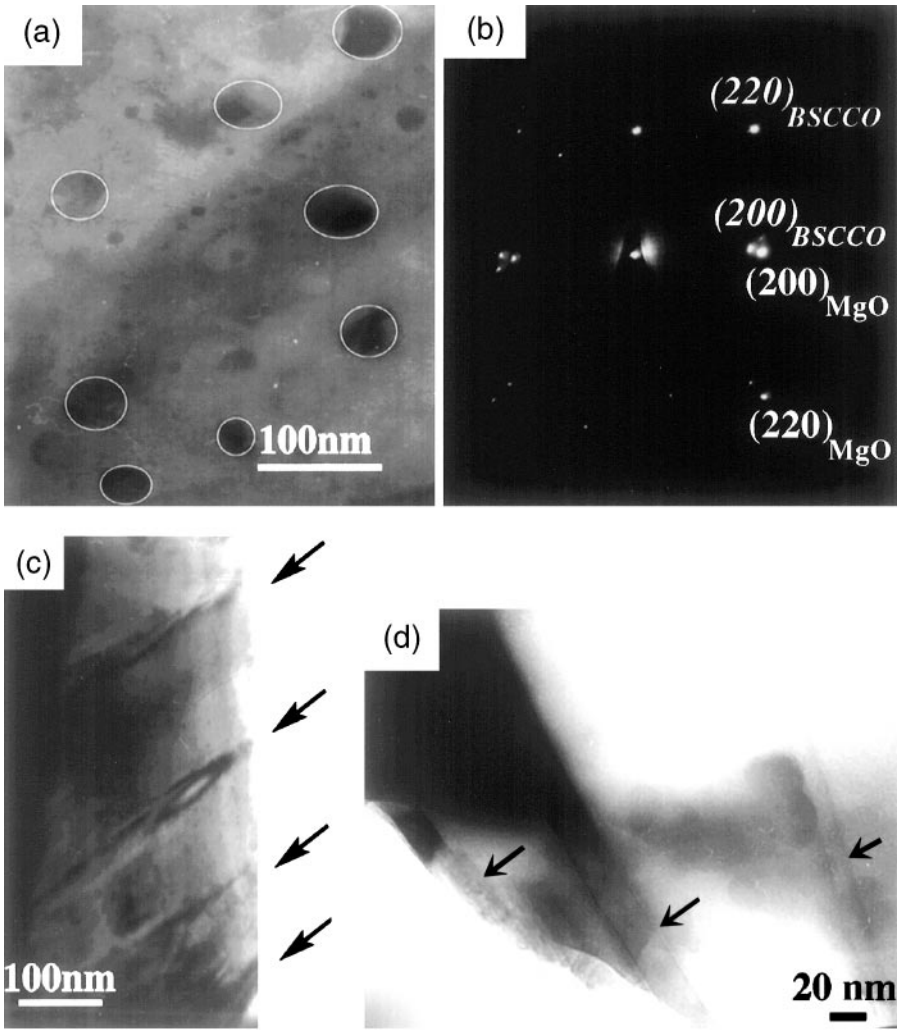

FIG. 14. (a) In-plane TEM micrograph of a bulk nanorod/BSCCO-2212 composite. The roughly circular dark spots correspond to MgO nanorods oriented perpendicular to the copper oxide planes. The in-plane density of rods is ca. $1 \times 10^{10}/\text{cm}^2$. (b) Selected area electron diffraction recorded on the sample shown in (a). Diffraction peaks corresponding to the in-plane BSCCO and MgO lattices are indexed. (c) TEM image of the sample after tilting the crystal off-axis. (d) TEM image showing several nanorods oriented parallel to the copper oxide planes; these nanorods are highlighted with arrows.

We have also directly assessed the stability of the MgO nanorods by making spatially resolved EDAX measurements across the nanorod/BSCCO-2212 interface. EDAX measurements indicate that there is a relatively sharp interface between the MgO nanorods and the BSCCO-2212 matrix with little interdiffusion and reaction. Figure 15(a) shows a TEM bright-field image of a typical, sharp nanorod/BSCCO interface. Figures 15(b) and 15(c) are typical EDAX spectra recorded across the nanorod/BSCCO-2212 interface using a 10 nm beam size. No Mg signal can be detected after moving several nm beyond the interface into the BSCCO matrix [Fig. 15(c)]. Backscattered electron imaging on composite surfaces further indicates there is little diffusion of Mg into the BSCCO-2212 lattice. These results demonstrate that the MgO nanorods are chemically compatible with BSCCO and maintain their structure after incorporation into this matrix.

C. Entrapment and self-organization of nanorods in the HTS matrix

The observed entrapment of MgO nanorods within BSCCO-2212 crystallites can be understood within the framework of pushing/trapping behavior of foreign particles at an advancing solid/liquid interface during solidification and crystallization. According to the Uhlmann–Chalmers–Jackson (UCJ) model,[41] the relative magnitude of the particle/solid (σ_{ps}), particle/liquid (σ_{pl}), and solid/liquid (σ_{sl}) interfacial free energies determines whether a particle is trapped or pushed out of the growth interface. At equilibrium, particle interaction

CAMBRIDGE JOURNALS
http://journals.cambridge.org Downloaded: 30 Oct 2015 IP address: 128.103.96.231

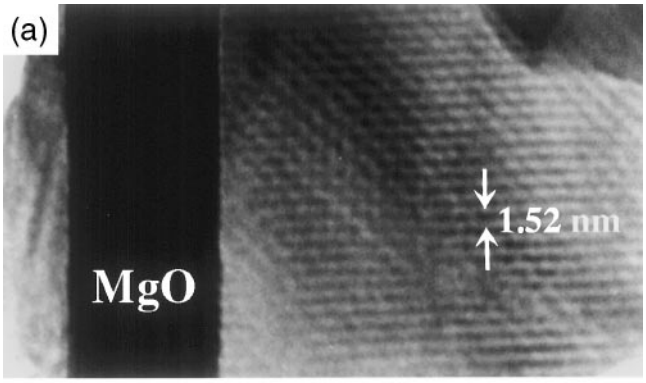

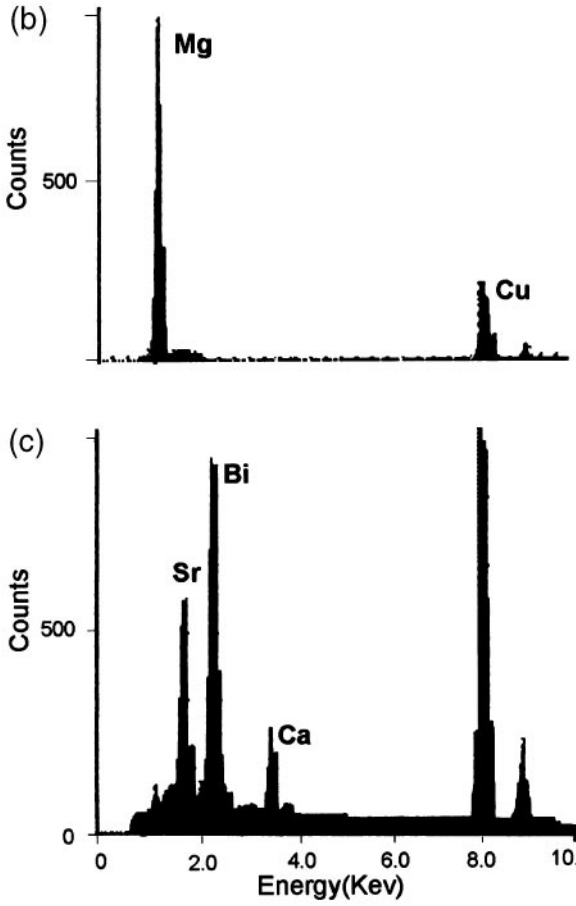

FIG. 15. (a) High-resolution TEM image obtained from the interface between a MgO nanorod and BSCCO-2212 bulk composite sample. (b) Typical EDAX spectrum recorded on the MgO nanorod region of the sample. (c) Typical EDAX spectrum recorded on the BSCCO region of the sample. The electron beam size was 10 nm in these experiments.

at the solid/liquid interface is given by

$$\sigma_{ps} = \sigma_{pl} + \sigma_{sl} . \quad (1)$$

When σ_{ps} is greater than the sum of σ_{pl} and σ_{sl}, the particle is pushed from the interface toward the liquid phase. In contrast, when σ_{ps} is less than the sum of σ_{pl} and σ_{sl}, the particle is trapped within the growing solid [Figs. 17(a) and 17(b)].

It has also been demonstrated that smaller particles are more easily pushed outside the solid in the Y-211/Y-123 system[42–45] where it is likely that $\sigma_{ps} > \sigma_{pl} + \sigma_{sl}$. Small Y-211 particles can be still be trapped in Y-123 if sufficiently high growth rates are used. Similarly, it is expected that very high crystal growth rates would be required to trap nanometer scale particles (i.e., nanorods) inside BSCCO grains if $\sigma_{ps} > \sigma_{pl} + \sigma_{sl}$. The fact that a large number of nanorods are incorporated under very modest growth rates suggest that this inequality does not hold for our system. Indeed, the relatively good epitaxial relationships between MgO and BSCCO-2212 suggest that the nanorods can serve as nucleation sites for crystal

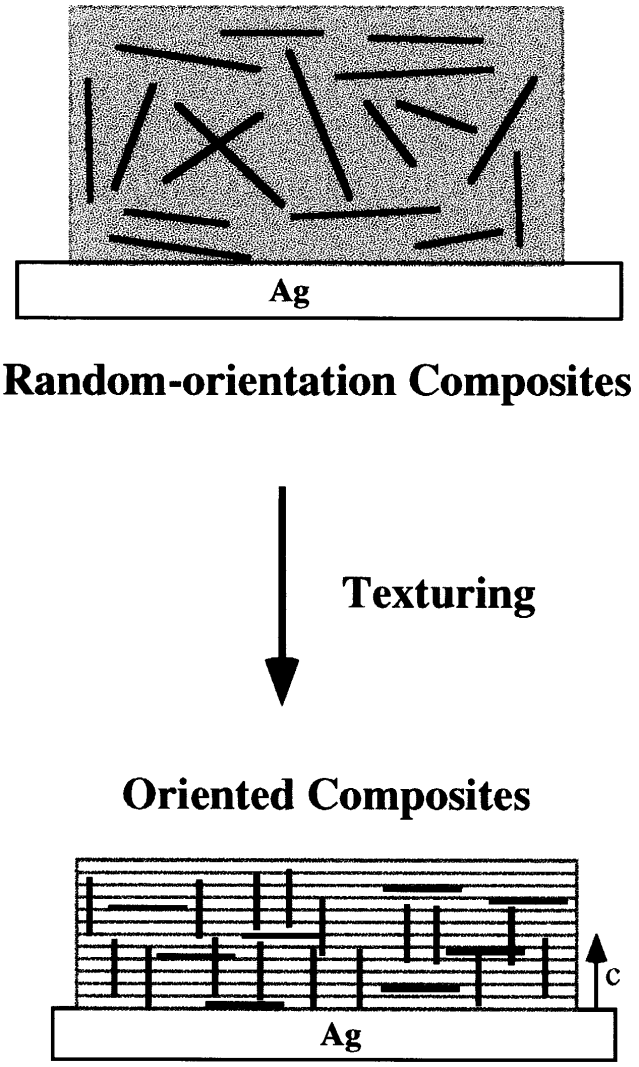

FIG. 16. Schematic diagram illustrating the self-organization of MgO nanorods in HTS grains. Self-organization is driven by lattice epitaxy.

CAMBRIDGE JOURNALS
http://journals.cambridge.org Downloaded: 30 Oct 2015 IP address: 128.103.96.231

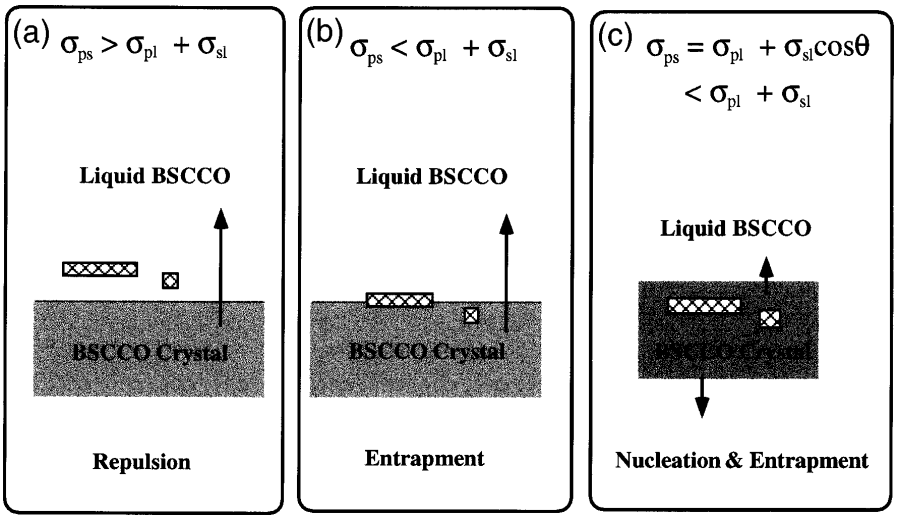

FIG. 17. Schematic diagrams showing the interaction of MgO nanorods and the HTS crystal growth front under three hypothetical conditions: (a) repulsion, (b) entrapment, and (c) nucleation and entrapment.

growth. In this case, we can rewrite Eq. (1) as

$$\sigma_{ps} = \sigma_{pl} + \sigma_{sl} \cos\theta , \qquad (2)$$

where θ is the wetting angle of the liquid, and thus we expect the MgO nanorods to be trapped regardless of their size [Fig. 17(c)].

The preferred orientation or self-organization of the MgO nanorods after melt-texturing is not surprising when we consider that the exposed MgO (110) and (001) surfaces are lattice-matched substrates for the growth of BSCCO with either its *a*- and *b*-axes or the *c*-axis oriented parallel to the nanorod axis. Indeed, (110) and (001) epitaxial growth has been widely documented in the literature.[46,47] Lastly, we note that the high anisotropy of the nanorods could also affect the trapping and organization within the HTS matrix and will need to be considered in the future.

D. Critical current densities of nanorod/HTS composites

We have systematically characterized J_c in the nanorod/HTS composites and HTS reference samples through measurements of the sample magnetization (M) as a function of magnetic field and temperature using the Bean model. In general, we see large enhancements of J_c for composite samples compared with the reference samples. Field-dependent J_c data determined at several temperatures for reference and composite BSCCO-2212 samples with nanorod densities of $3 \times 10^9/\text{cm}^2$ and $2 \times 10^{10}/\text{cm}^2$ are shown in Fig. 18. The nanorod/BSCCO-2212 composites exhibit large increases in J_c compared with the reference samples, and these increases are especially significant at higher magnetic fields and temperatures. Because the J_c values of our BSCCO-2212 reference samples are comparable to the best reported for polycrystalline thick films,[17,21] we believe that the increases observed in the nanorod composites are not an artifact of our chosen reference point.

The large increases in J_c are attributed to enhanced pinning arising from nanorod columnar defects in our composite samples. Several pieces of evidence support this proposal. First, the increases in $J_c(H, T)$ become more pronounced with increasing field and temperature. These results are characteristic of the behavior expected for pinning by columnar defects and cannot be explained by point-defect pinning, since point defect pinning is weak above 30 K. Second, our previous studies have shown that the enhancement in J_c exhibits an inverse dependence on the average diameter of the nanorods.[26] These results are consistent with expectations for optimal pinning,[14] and also show the importance of developing small nanorods for the HTS composites in order to achieve the optimal pinning efficiency.[45] Third, the present results demonstrate that higher nanorod densities yield larger J_c's at elevated fields, as expected for flux line pinning by columnar defects.

We examined the temperature dependence of J_c for selected magnetic field values to evaluate the potential of these composites for applications. Results obtained on nanorod/BSCCO-2212 composite and reference samples at $H = 0.3$ and 0.5 T are shown in Fig. 19; the composite sample has a nanorod density of $2 \times 10^{10}/\text{cm}^2$. In the reference samples, J_c fell off rapidly with temperature as a result of TAFF. In the nanorod/BSCCO composites, however, this rapid fall-off was dramatically reduced and led to improvements in J_c that could exceed one order of magnitude. The large increases in $J_c(H, T)$ for the

CAMBRIDGE JOURNALS
http://journals.cambridge.org Downloaded: 30 Oct 2015 IP address: 128.103.96.231

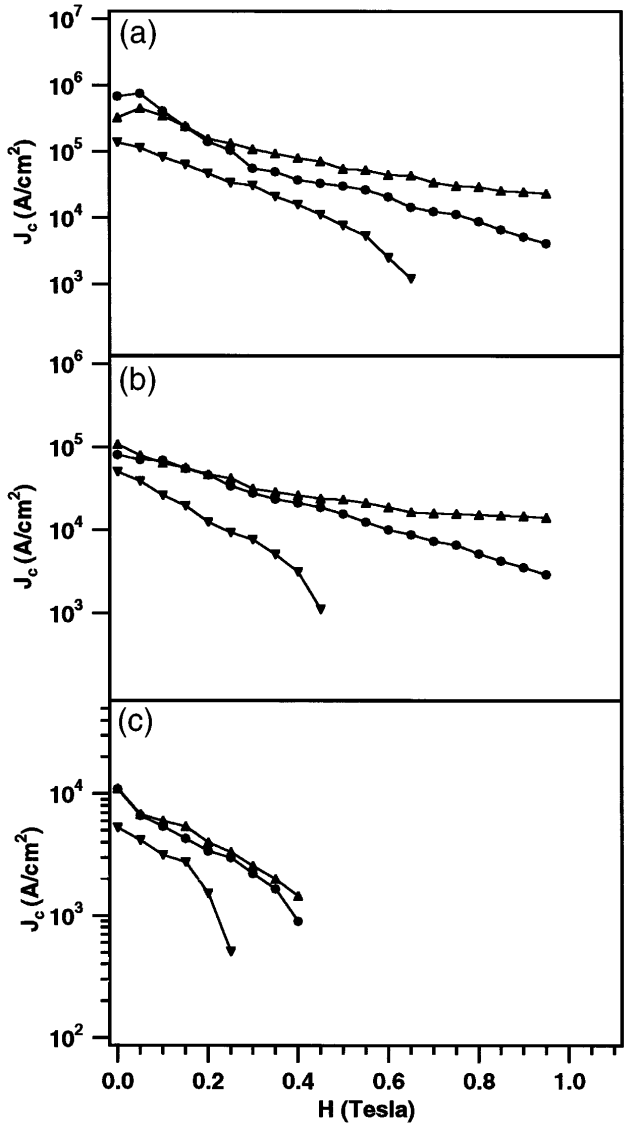

FIG. 18. Comparison of the magnetic field dependence of J_c for nanorod/BSCCO-2212 composites formed with nanorod densities of $3 \times 10^9/\text{cm}^2$ (●) and $2 \times 10^{10}/\text{cm}^2$ (▲), and a BSCCO reference (▼). The data were recorded at (a) 20, (b) 40, and (c) 60 K. The T_c's of all three samples were 80 K.

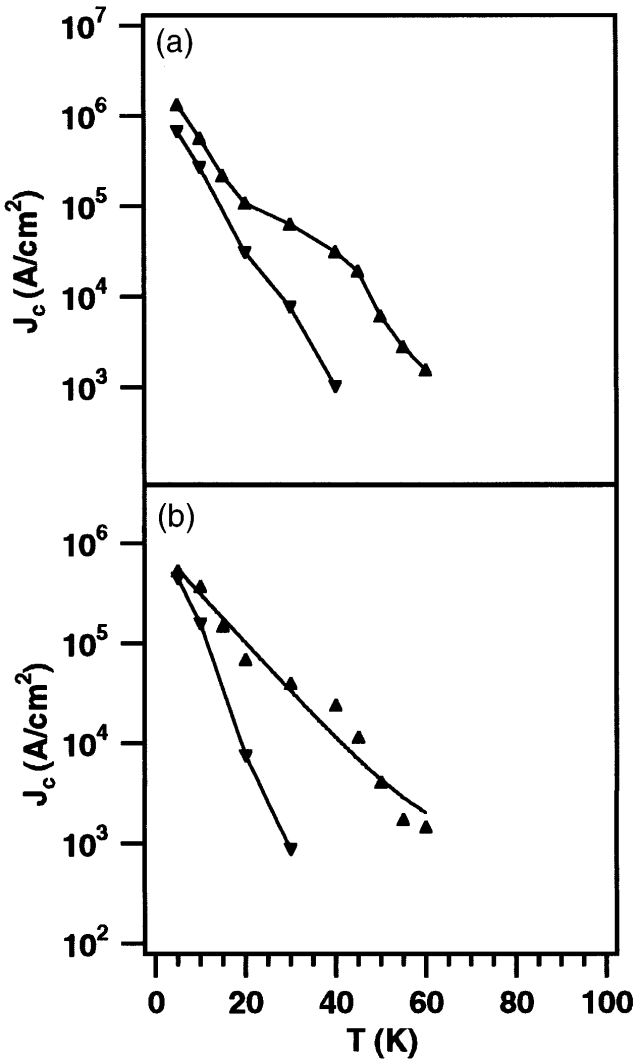

FIG. 19. Comparison of the temperature dependence of J_c in typical nanorod/BSCCO-2212 composite (▲) and reference (▼) samples at (a) 0.3 and (b) 0.5 T. The nanorod density in the composite was $2 \times 10^{10}/\text{cm}^2$.

nanorod/BSCCO-2212 composites can also be summarized by a plot of the irreversibility line[21] in the magnetic field-temperature plane (Fig. 20). From the standpoint of applications, the operating field and temperature must be chosen to be below this line because dissipation (that is, loss of superconductivity) occurs above it. In our studies, the irreversibility point was taken as the field at which the magnetization hysteresis loop closed for each temperature. The closing criterion was taken to be 5×10^{-5} electromagnetic units and was applied to similar-sized composite and reference samples in the analysis. Large upward shifts in the irreversibility line for the nanorod/BSCCO-2212 composites are observed. Indeed, the composite containing the highest density ($2 \times 10^{10}/\text{cm}^2$) of nanorods exhibits shifts of 23 and 30 K at fields of 0.5 and 1.0 T, respectively. We can thus conclude that the potential operating regime for BSCCO-2212 is extended significantly by formation of the nanorod composite.

Similar results have been obtained on nanorod/TBCCO-2223 systems as well. Figure 21 shows the field dependence of J_c determined at several temperatures for reference and composite samples. In general, the nanorod/TBCCO-2223 composites exhibit large in-

CAMBRIDGE JOURNALS
http://journals.cambridge.org Downloaded: 30 Oct 2015 IP address: 128.103.96.231

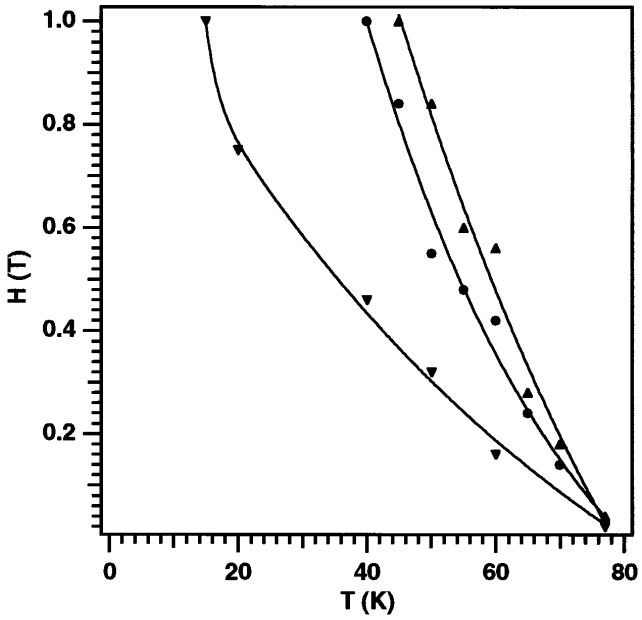

FIG. 20. Plots of the irreversibility lines for nanorod/BSCCO-2212 composites with nanorod densities of $3 \times 10^9/\text{cm}^2$ (●) and $2 \times 10^{10}/\text{cm}^2$ (▲), and a BSCCO reference (▼) sample.

creases in J_c compared with the reference samples, and these increases are especially significant at elevated fields and temperatures. The explicit temperature dependencies of J_c obtained on nanorod/TBCCO composite and reference samples at 0.5 and 0.8 T are shown in Fig. 22. J_c typically was found to drop more rapidly with temperature in the reference compared to the composite samples. Lastly, the large increases in $J_c(H, T)$ for the nanorod/TBCCO-2223 composites have been summarized by a plot of the irreversibility line in Fig. 23. Significantly, we observe large upward shifts in the irreversibility line for the nanorod/TBCCO composites: 30 and 35 K at fields of 0.5 and 1.0 T, respectively. These upward shifts in the irreversibility line are comparable to our observations in BSCCO and demonstrate the generality of our approach to different HTS materials.

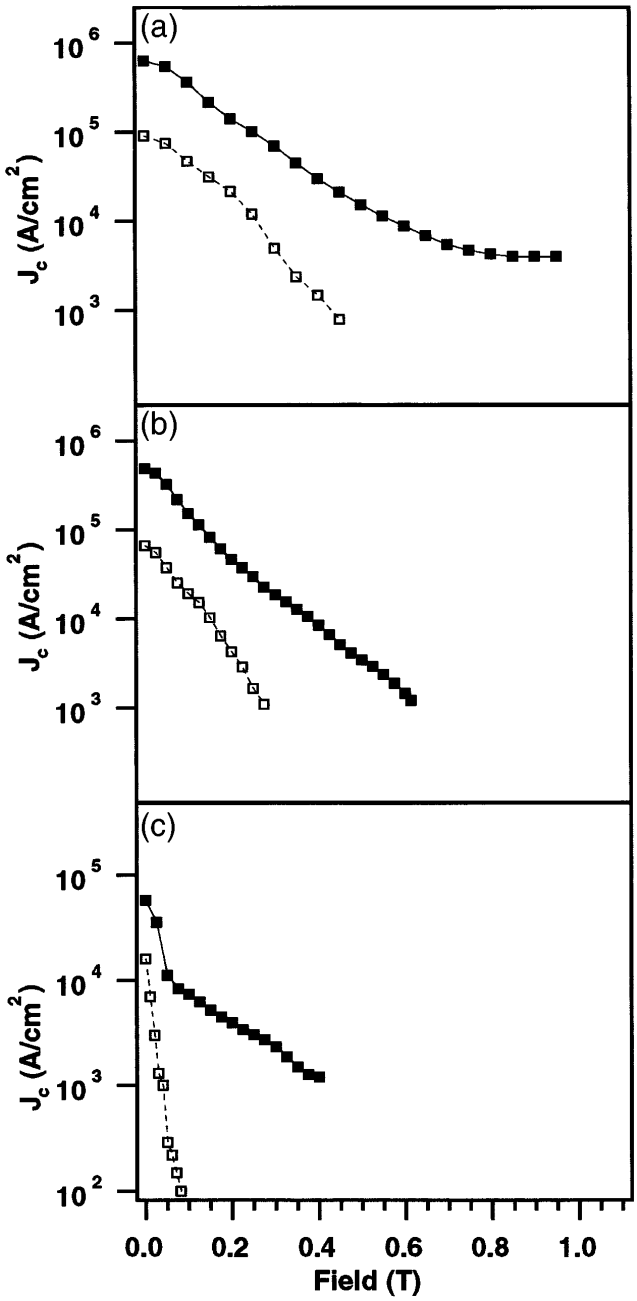

FIG. 21. Comparison of the field dependence of J_c for a typical nanorod/TBCCO-2223 composite with a nanorod density of $3 \times 10^9/\text{cm}^2$ (■) and a typical TBCCO reference (□). The data were recorded at (a) 50, (b) 60, and (c) 90 K. The T_c's of both samples were 120 K.

IV. CONCLUSIONS

A chemical approach to the formation of columnar defects has been developed involving the growth of MgO nanorods and subsequent incorporation of these rod-like nanostructures into HTS's to form nanorod/superconductor composites. MgO nanorods have been successfully incorporated into $Bi_2Sr_2CaCu_2O_z$, $Bi_2Sr_2Ca_2Cu_3O_z$, and $Tl_2Ba_2Ca_2Cu_3O_z$ superconductors at densities up to $2 \times 10^{10}/\text{cm}^2$. Microstructural analyses of the composites demonstrate that the MgO nanorods (1) create a columnar defect structure in the HTS matrices, (2) form a compositionally sharp interface with the matrix, and (3) self-organize into orientations perpendicular and parallel to the HTS copper oxide planes. A model incorporating entrapment and lattice epitaxy has been used to understand these observations. Measurements of the critical current density as a function of temperature and field demonstrate that the MgO nanorod/HTS

CAMBRIDGE JOURNALS
http://journals.cambridge.org Downloaded: 30 Oct 2015 IP address: 128.103.96.231

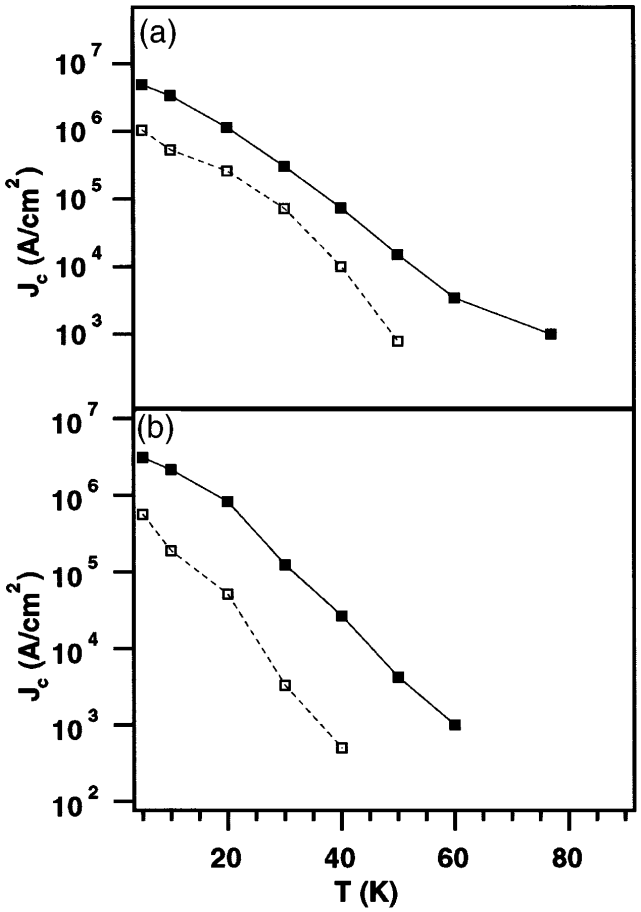

FIG. 22. Comparison of the temperature dependence of J_c in a typical nanorod/TBCCO-2223 composite with a nanorod density of $3 \times 10^9/\text{cm}^2$ (■) and a TBCCO reference sample (□) at (a) 0.5 and (b) 0.8 T.

composites exhibit significant enhancements at elevated temperatures and magnetic fields compared with reference samples. These enhancements in J_c lead to large upward shifts in the irreversibility line for the composites, and thus show that the operating regime of these HTS materials can be extended significantly through the incorporation of nanorods. Because MgO nanorods can be incorporated into HTS's using current processing schemes, these results suggest that the nanorod/HTS composites may represent a technologically viable strategy for increasing critical currents in large-scale applications.

ACKNOWLEDGMENTS

We acknowledge helpful discussions with D. R. Nelson, F. Spaepen, and Y. Lu. This work was supported in part by the Office of Naval Research and the Materials Research Science and Engineering Center Program of the National Science Foundation.

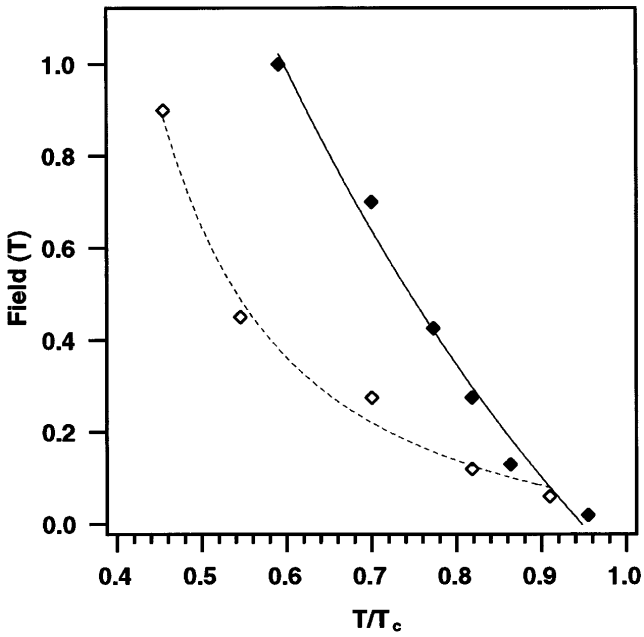

FIG. 23. Plots of the irreversibility lines for nanorod/TBCCO-2223 composites with nanorod densities of $3 \times 10^9/\text{cm}^2$ (◆) and TBCCO reference samples (◇).

REFERENCES

1. G. B. Lubkin, Phys. Today **49**, 48 (1996).
2. P. M. Grant, Nature **375**, 107 (1995).
3. D. C. Larbalestier, Science **274**, 736 (1996).
4. D. J. Bishop, P. L. Grammel, D. A. Huse, and C. A. Murray, Science **255**, 165 (1992).
5. D. S. Fisher, M. P. A. Fisher, and D. A. Huse, Phys. Rev. B **43**, 130 (1991).
6. G. Blatter, M. V. Feigelman, V. B. Geshkenbein, A. I. Larkin, and V. M. Vinokur, Rev. Mod. Phys. **66**, 1125 (1994).
7. M. Polak, J. A. Parrell, A. A. Polyanskii, A. E. Pashitski, and D. C. Larbalestier, Appl. Phys. Lett. **70**, 1034 (1997).
8. U. Welp, D. O. Gunter, G. W. Crabtree, W. Zhong, U. Balachandran, P. Haldar, R. S. Sokolowski, V. K. Vlasko-Vlasov, and N. Nikitenko, Nature **376**, 44 (1995).
9. D. P. Norton, A. Goyal, J. D. Budai, D. K. Christen, D. M. Kroeger, E. D. Specht, Q. He, B. Saffian, M. Paranthaman, C. E. Klabunde, D. F. Lee, B. C. Sales, and F. A. List, Science **274**, 755 (1996).
10. P. M. Grant, Nature **381**, 559 (1996).
11. D. C. Larbalestier, X. Y. Cai, Y. Feng, H. Edelman, A. Umezawa, G. N. Riley, Jr., and W. L. Carter, Physica C **221**, 299 (1994).
12. Q. Li, H. J. Wiesman, M. Suenaga, L. Motowidlo, and P. Haldar, Appl. Phys. Lett. **66**, 637 (1995).
13. P. Majewski, Adv. Mater. **6**, 593 (1994).
14. D. R. Nelson and V. M. Vinokur, Phys. Rev. Lett. **68**, 2398 (1992).
15. T. Hwa, P. Le Doussal, D. R. Nelson, and V. M. Vinokur, Phys. Rev. Lett. **71**, 3545 (1993).
16. L. Civale, A. D. Marwick, T. K. Worthington, M. A. Kirk, J. R. Thompson, L. Krusin-Elbaum, Y. Sun, J. R. Clem, and F. Holtzberg, Phys. Rev. Lett. **67**, 648 (1991).
17. R. C. Budhani, M. Suenaga, and S. H. Liou, Phys. Rev. Lett. **69**, 3816 (1992).
18. M. Konczykowski, N. Chikumoto, V. Vinokur, and M. V. Feigel'man, Phys. Rev. B **51**, 3957 (1995).

CAMBRIDGE JOURNALS
http://journals.cambridge.org Downloaded: 30 Oct 2015 IP address: 128.103.96.231

19. Y. Zhu, Z. X. Cai, R. C. Budhani, M. Suenaga, and D. O. Welch, Phys. Rev. B **48**, 6436 (1993).
20. J. R. Thompson, D. Paul, Z. L. Wang, D. M. Kroeger, and D. K. Christen, Appl. Phys. Lett. **67**, 1007 (1995).
21. L. Krusin-Elbaum, J. R. Thompson, R. Wheeler, A. D. Marwick, C. Li, S. Patel, D. T. Shaw, P. Lisowski, and J. Ullmann, Appl. Phys. Lett. **64**, 3331 (1994).
22. H. Safar, J. H. Cho, S. Fleshler, M. P. Maley, J. O. Willis, J. Y. Coulter, J. L. Ullmann, P. W. Lisowski, G. N. Riley, Jr., M. W. Rupich, J. R. Thompson, and L. Krusin-Elbaum, Appl. Phys. Lett. **67**, 130 (1995).
23. P. Le Doussal and D. R. Nelson, Physica C **232**, 69 (1994).
24. K. Fossheim, E. D. Tuset, T. W. Ebbessen, M. M. J. Treasy, and J. Schwarz, Physica C **248**, 195 (1995).
25. H. Dai, E. Wong, Y. Lu, S. Fan, and C. M. Lieber, Nature **375**, 769 (1995).
26. P. Yang and C. M. Lieber, Science **273**, 1836 (1996).
27. N. Adamopoulos, B. Soylu, Y. Yan, and J. E. Evetts, Physica C **242**, 68 (1993).
28. Y. S. Yuan, M. S. Wong, and S. S. Wang, J. Mater. Res. **11**, 8 (1996).
29. P. Yang and C. M. Lieber, Appl. Phys. Lett. **70**, 3158 (1997).
30. C. M. Lieber and P. Yang, patent pending, Ser. No. #08/606,892.
31. H. Itoh, S. Utamapanya, J. V. Stark, K. J. Klabunde, and J. R. Schlup, Chem. Mater. **5**, 71 (1993).
32. A. Morales, P. Yang, and C. M. Lieber, J. Am. Chem. Soc. **116**, 8360 (1994).
33. C. Li, S. Patel, J. Ye, E. Narumi, D. T. Shaw, and T. Sato, Appl. Phys. Lett. **63**, 2558 (1993).
34. T. Brousse, G. Poullain, J. F. Hamet, H. Murray, and B. Raveau, Physica C **170**, 545 (1990).
35. H. Tabata, T. Kawai, M. Kanai, O. Murata, and S. Kawai, Jpn. J. Appl. Phys. **28**, L430 (1989).
36. W. L. Holstein and L. A. Parisi, J. Mater. Res. **11**, 1349 (1996).
37. C. P. Bean, Rev. Mod. Phys. **36**, 31 (1964).
38. W. B. Campbell, in *Whisker Technology*, edited by A. P. Levitt (Wiley, New York, 1990), p. 15.
39. E. G. Wolff and T. D. Coskren, J. Am. Ceram. Soc. **48**, 279 (1965).
40. J. V. Stark, D. G. Park, I. Lagadic, and K. J. Klabunde, Chem. Mater. **8**, 1904 (1996).
41. D. R. Uhlmann, B. Chalmers, and K. A. Jackson, J. Appl. Phys. **35**, 2986 (1964).
42. Y. Nakamura, A. Endo, and Y. Shiohara, J. Mater. Res. **11**, 1094 (1996).
43. C. Kim, K. Kim, G. Hong, and H. Lee, J. Mater. Res. **10**, 1605 (1995).
44. A. Endo, H. Chauhan, T. Egi, and Y. Shiohara, J. Mater. Res. **11**, 795 (1996).
45. M. Murakami, Prog. Mater. Sci. **38**, 311 (1994).
46. Y. Nagai and K. Tsuru, Jpn. J. Appl. Phys. **29**, L1600 (1990).
47. M. Ohkuho, E. Brecht, G. Linker, J. Geerk, and O. Meyer, Appl. Phys. Lett. **69**, 574 (1996).

CAMBRIDGE JOURNALS
http://journals.cambridge.org Downloaded: 30 Oct 2015 IP address: 128.103.96.231